Simultaneous Multipass Resistive-Pulse Sensing and Fluorescence Imaging of Liposomes

Alexandra J. Schmeltzer[1], Eric M. Peterson[2], Daniel K. Lathrop[2], Sean R. German[2], and Henry S. White[1*]*

[1]Department of Chemistry, University of Utah; Salt Lake City, UT 84112, USA
[2]Electronic BioSciences, Inc., 421 Wakara Way, Suite 328, Salt Lake City, UT 84108, USA
[*]Correspondence to: sgerman@electronicbio.com, white@chem.utah.edu

ABSTRACT

Simultaneous multipass resistive-pulse sensing and fluorescence imaging have been used to correlate the size and fluorescence intensity of individual *E. coli* lipid liposomes composed of *E. coli* polar lipid extract labeled with membrane-bound 3,3-dioctadecyloxacarbocyanine (DiO) fluorescent molecules. Here, a nanopipette serves as a waveguide to direct excitation light to the resistive-pulse sensing zone at the end of the nanopipette tip. Individual DiO-labeled liposomes (>50 nm radius) were multipassed back and forth through the orifices of glass nanopipettes 110-to-150 nm radius via potential switching to obtain sub-nanometer sizing precision, while recording the fluorescence intensity of the membrane-bound DiO molecules. Fluorescence was measured as a function of liposome radius and found to be approximately proportional to the total membrane surface area. The observed relationship between liposome size and fluorescence intensity suggests that multi-vesicle liposomes emit greater fluorescence compared to unilamellar liposomes, consistent with all lipid membranes of the multi-vesicle liposomes containing DiO. Fluorescent and non-fluorescent liposomes are readily distinguished from each other in the same solution using simultaneous multipass resistive-pulse sensing and fluorescence imaging. A fluorescence 'dead zone' of ~1 μm thickness just outside of the nanopipette orifice was observed during resistive-pulse sensing, resulting in 'on/off' fluorescent behavior during liposome

multipassing. Our results provide a path forward to simultaneously characterize the size of biologically relevant nanoparticles (*e.g.*, extracellular vesicles) and the presence of fluorescently labeled surface proteins.

KEYWORDS

resistive-pulse sensing, Coulter-counter, nanopipette, fluorescence, liposomes, cryoTEM

Extracellular vesicles (EVs) are small, cell-derived unilamellar liposomes that contain biomolecules both in the interior of the liposome (*e.g.*, DNA, RNA, proteins), in addition to membrane bound proteins on their exterior.[1] Recent studies suggest that the contents of EVs are directly correlated with their physical size.[2-4] Zhang et al. proposed a correlation between the size of EVs derived from AsPC-1 human pancreatic cancer and MDA-MB-231-4175 human breast cancer cell lines and their contents consisting of proteins, lipids, DNA, and RNA.[3] They reported diverse organ bio-distribution patterns for cancer-derived EVs of different sizes in mouse models and proposed biological functions of the EVs based on vesicle content and location within the body.[3] This work required the use of several analytical techniques, including field flow fractioning, light scattering, transmission electron microscopy, and nucleic acid analysis, to separate and characterize the EV subpopulations. Characterizing the contents of cancer-derived EVs on a vesicle-by-vesicle basis to identify subpopulations is critical to understanding disease progression and treatment, hence, there is a need for a method capable of extreme sizing precision with the ability to probe uniquely targetable characteristics, such as fluorescently labeling specific surface proteins. Herein, we report simultaneous multipass resistive-pulse sensing and fluorescence imaging to characterize biologically relevant model liposomes based on their size and the presence of fluorescent markers.

Coulter-counter or resistive-pulse sensing is widely used to characterize particle size, charge, shape, and concentration.[5-19] Resistive-pulse sensing was introduced in 1951 as an automated technique to count and size red blood cells, and is still commonly used today.[20-26] In resistive-pulse sensing, a cell or particle is detected as it passes through an opening separating two ionically conductive solutions by partially blocking the electrical current established between the electrodes placed on each side of the opening. In this work, the orifice of a laser-pulled glass nanopipette is used to resistively sense the translocations of liposomes as they enter and leave the nanopipette. Recent biological applications of resistive-pulse sensing include the characterization of exosomes originating from the MDA-MB-231 breast cancer cell line,[27, 28] delivery of liposomes containing redox active species to electrode surfaces,[29, 30] deformation measurements of multilamellar liposomes[31] and pseudo-type human immunodeficiency virus (HIV-1),[32] and characterization of DNA.[33, 34]

The characterization of biologically relevant particles via resistive-pulse sensing generally has limited sizing precision when translocating the particle one time through an opening separating two electrolyte solutions. While single passing particles enable high throughput measurements, there is ~15% error in the measured size based on a single translocation.[8] This error is due to variations in the position of the particle as it passes through the sensing zone.[16, 35] Particle translocation near the edge of nanopipette results in slightly larger resistive pulse blockage currents compared to particle translocation through the center of the nanopipette.[16, 35] To overcome this source of error in the resistive pulse measurements, multipassing particles through the nanopipette orifice many times enables extremely high precision measurements of the particle size.[8] For example, multipassing a single 250 nm radius polystyrene (PS) particle as few as 10 times reduces the standard error (SE) of the measurement

to less than 1 nm.[8] The application of multipass resistive-pulse sensing to characterize biologically relevant particles (*e.g.*, liposomes and EVs) would enable precise sub-nanometer size characterization on an individual particle basis. Combining fluorescence imaging with multipass resistive-pulse sensing enables simultaneous sub-nanometer sizing precision and the detection of fluorescent markers on the surface of biologically relevant particles. Fluorescent markers are commonly used to detect specific proteins on the surface of a biological particle.[36] The combination of these two methods provides a powerful means to simultaneously characterize the presence of surface proteins and the size of biological particles.

Previously, fluorescence imaging has been used simultaneously with resistive-pulse sensing for studies of single passed fluorescently labeled DNA,[37-39] H_2 formation on single freely diffusing photoactive 40 nm Ag nanoparticles,[40] and single passed fluorescent PS nanoparticles 2 μm in diameter.[41] Yu et al. used fluorescent PS nanoparticles (diameter = 260 and 540 nm) to track the Brownian motion of nanoparticles upon exiting a nanopipette.[42] In this latter study, an external excitation light source was used to illuminate nanoparticles to obtain the diffusional paths outside of the nanopipette, where limited pressure-driven particle multipassing was reported in order to obtain multiple diffusional paths of the same particle.[42]

In our current study of fluorescently labeled liposomes, the excitation light is delivered through the cleaved end of a single-mode optical fiber located within the nanopipette (positioned ~1 mm from the nanopipette orifice) to illuminate the liposomes inside the nanopipette (Figure 1). The nanopipette is filled with electrolyte solution and an internal Ag/AgCl electrode is placed inside of the nanopipette. The illuminated tip of the nanopipette is submerged in the electrolyte solution and positioned above the objective of an inverted microscope. This scheme takes advantage of the waveguide properties of the nanopipette to automatically direct illumination to

the tip and thus does not suffer from fluctuations in excitation intensity at the small tip due to mechanical drift or vibration of the nanopipette relative to the position of external illumination source. A second external Ag/AgCl is placed in the bulk electrolyte solution exterior to the nanopipette. The potential of the external Ag/AgCl electrode is alternated between positive and negative potential (typically ±1 V) with respect to the internal electrode to drive liposome multipassing.[9] The fluorescence emission (≥ 500 nm) of the DiO molecules within the liposome membrane is recorded during multipassing. A photograph of the experimental setup is shown in the Supporting Information (Figure S1).

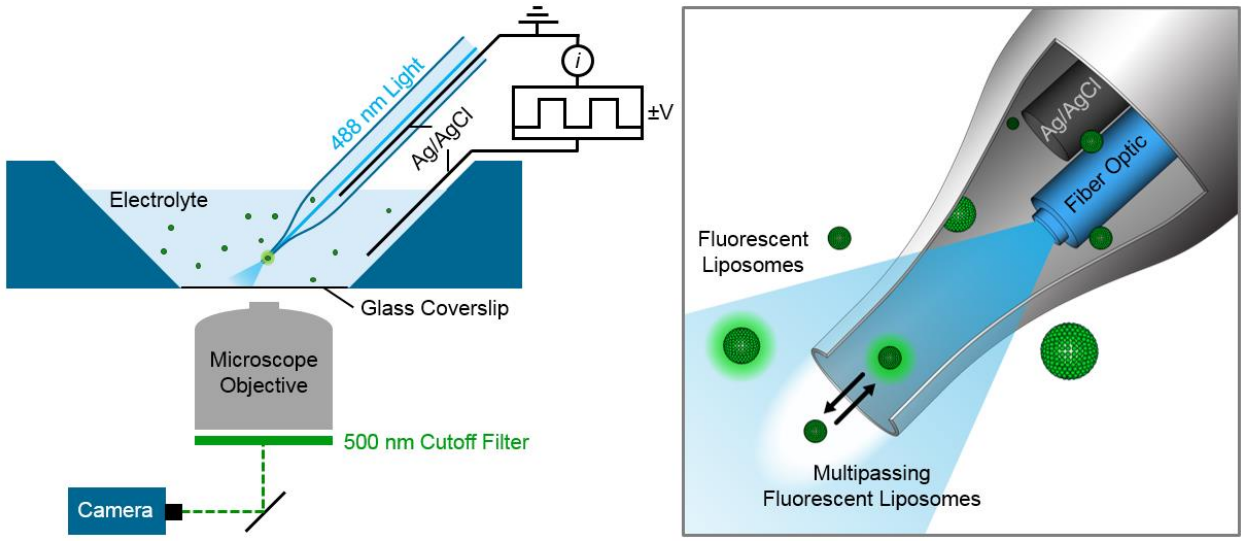

Figure 1. Diagram of the experimental setup. A glass nanopipette filled with electrolyte containing an internal Ag/AgCl electrode, and a fiber optic (λ_{ex} = 488 nm, 2 mW power) is positioned above an inverted microscope objective at a 45^{o} angle. A second Ag/AgCl electrode is positioned in the external electrolyte solution. Fluorescence imaging is recorded using a sCMOS camera attached to the base of the inverted microscope. Fluorescent DiO-labeled *E. coli* lipid liposomes ($\lambda_{em} \geq 500$ nm) are multipassed through the orifice of a nanopipette tip (110-to-150 nm radius) to quantify liposome size and fluorescence signal. Figure is not drawn to scale.

RESULTS AND DISCUSSION

Simultaneous multipass resistive-pulse sensing and fluorescence imaging of DiO-labeled *E. coli* lipid liposomes. The driving force responsible for multipassing particles through the orifice of a nanopipette is the sum of the potential dependent electrokinetic forces acting upon the particle.[5, 43] An electroosmotic force arises from solution flow induced by the diffuse double-layer formed on the negatively charged glass surface of the nanopipette, and an electrophoretic force arises from the negative charge of the *E. coli* lipid liposome surface.[5, 43] At positive potentials (external electrode *vs*. internal electrode) the electroosmotic force is directed into the pipette and the electrophoretic force is directed out of the pipette, while at negative potentials the directions of the two electrokinetic forces are reversed. Both the electroosmotic and electrophoretic forces increase with increasing applied potential, resulting in increased particle velocity during translocations.[5, 43] The primary force driving liposome multipassing in this study is electrophoresis, which determines the direction of the liposome transport.

When a liposome translocates through the orifice of the nanopipette, a portion of the electrical current is blocked due to volume exclusion corresponding to the physical size of the liposome. This blockage current is called a resistive pulse. The resistive pulses indicate when the liposome has entered and left the nanopipette during potential-driven multipassing. Activation of the applied potential to drive liposome motion is triggered by a field programmable gate array (FPGA) that monitors the *i-t* trace for a resistive pulse and commands the potential to be switched after a set delay time (2–10 ms) following particle translocation. The distance the liposome travels into and out of the nanopipette tip is related to the internal and external delay times, respectively (Figure S2). Shorter, ≤ 5 ms, external delay times are preferred during

multipassing to decrease the likelihood of the liposome diffusing too far away into the external electrolyte solution for recapture.

Figure 2 shows the simultaneous resistive-pulse sensing and fluorescence imaging of a single fluorescent *E. coli* lipid liposome multipassed 5 times through the orifice of a 111 ± 8 nm radius nanopipette. The applied potential waveform (Figure 2A) drives the liposome transport in and out of the nanopipette, with the liposome entering at -1.0 V and leaving at 1.0 V. The red shading in Figure 2 indicates when the liposome is outside of the nanopipette and the blue shading is when the liposome is inside of the nanopipette. The resistive pulses associated with liposome multipassing are shown in the *i-t* trace of Figure 2B.

The fluorescence emission of the liposome is recorded simultaneously with resistive-pulse sensing (Figure 2C). The fluorescence signals reported in this work were obtained by defining a 5.4 × 5.4 μm (18 × 18 pixel) region of interest (ROI) located at the end of the nanopipette to quantify the fluorescence intensity of a multipassing liposome (Figure 3 and Figure S3). The fluorescence intensity is recorded in analog-to-digital units (ADU) and converted to the number of photons by calibrating the camera detector gain from a series of gradient images.[43] Details regarding the conversion are shown in Figure S4. We observed that the liposomes do not emit fluorescence when located directly outside of the nanopipette orifice resulting in liposomes displaying 'on/off' fluorescence behavior during multipassing, as discussed in a later section. A supplementary video has been provided showing the multipassing of a fluorescent liposome at 10 fps (200× slower than real time) (Video S1).

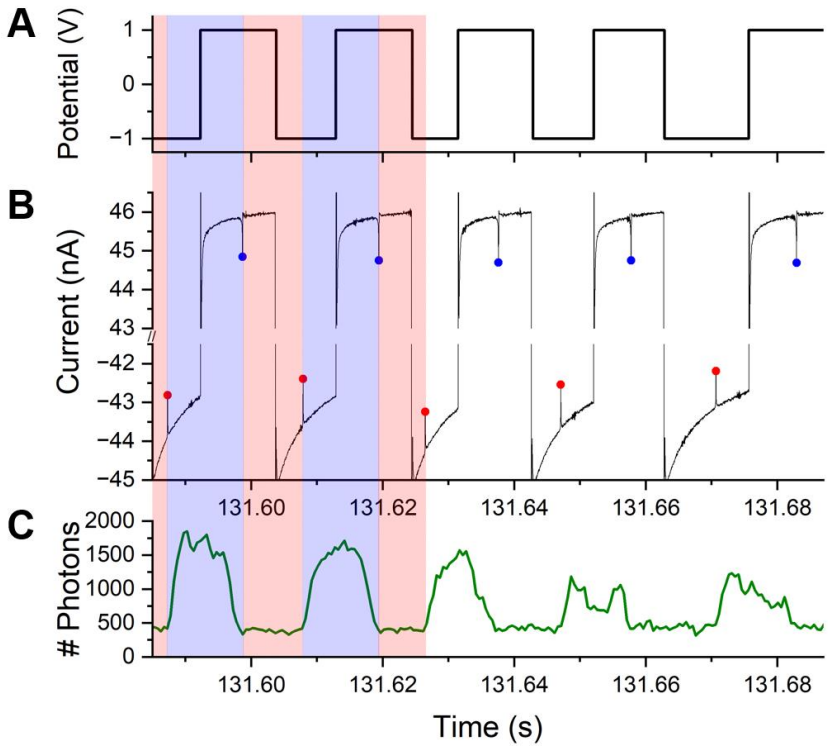

Figure 2. Simultaneous multipass resistive-pulse sensing and fluorescence imaging. (A) An individual 105.5 ± 0.5 nm radius liposome is multipassed back and forth through a nanopipette orifice 5 times by applying an alternating potential of ±1.0 V relative to the external Ag/AgCl. (B) The *i-t* trace contains resistive pulses corresponding to when the liposome enters (red points) and leaves (blue points) the nanopipette in response to the applied potential. (C) The fluorescence *vs.* time trace recorded simultaneously with the *i-t* trace. The liposome fluoresces when it is inside of the nanopipette tip (blue shading) and no fluorescence is observed when it is outside of the nanopipette (red shading). Potential switching delay times of 5 ms were used. The solution contained 0.1 M NaCl, and 10 mM PB (pH 7). Nanopipette radius = 111 ± 8 nm.

Figure 3A and 3B show representative expanded *i-t* traces of resistive pulses corresponding to a liposome entering and leaving the nanopipette at -1.0 V and +1.0 V, respectively. The asymmetric shape of the resistive pulse arises from the conical shape of the

nanopipette and indicates the direction that the liposome is traveling when translocating through the orifice. [4, 5, 8, 9, 44-46] A resistive pulse corresponding to a liposome entering the nanopipette exhibits a sharp decrease in current at the leading edge of the pulse, indicating when the liposome first passes through the nanopipette orifice. The current gradually returns to the open-nanopipette baseline current as the liposome travels up into the conically-shaped nanopipette and no longer blocks the orifice (Figure 3A). The opposite shape is observed for a liposome exiting the nanopipette, where the leading edge of the resistive pulse is gradual as the liposome travels down the nanopipette, followed by a sharp increase in current back to the baseline as the liposome exits the nanopipette orifice (Figure 3B).[44, 45] The baseline currents of the *i*-*t* traces were fit using asymmetric least squares shown by the dashed orange line in Figures 3A and 3B (see Supporting Information). The charging current following potential switching results in non-linear baseline currents.[8] The asymmetric least squares fit to the baseline current is used to calculate the maximum blockage current of a liposome translocation (Figure S5).

Figure 3C shows fluorescent images and a schematic of a single DiO-labeled *E. coli* lipid liposome translocating in and out of a nanopipette. The first panel of Figure 3C corresponds to the liposome located directly outside of the nanopipette and not fluorescing. At the time of this image, the resistive-pulse trace indicated that the liposome had left the nanopipette but had not yet been recaptured. We are unable to track the exact location of the liposome due to the lack of fluorescence, but based on the resistive pulses it is known that the liposome is outside of the nanopipette presumably near the orifice. The sequential images show the liposome entering into the nanopipette and emitting fluorescence, followed by the fluorescing liposome traveling ~2 μm into the nanopipette tip at -1.0 V before the potential is switched to 1.0 V, driving the liposome back towards the nanopipette opening. The approximate location of the nanopipette tip is shown

in the first panel of Figure 3C. Figure S3 shows example brightfield images of fluorescent particles first entering the nanopipette where the nanopipette is visible.

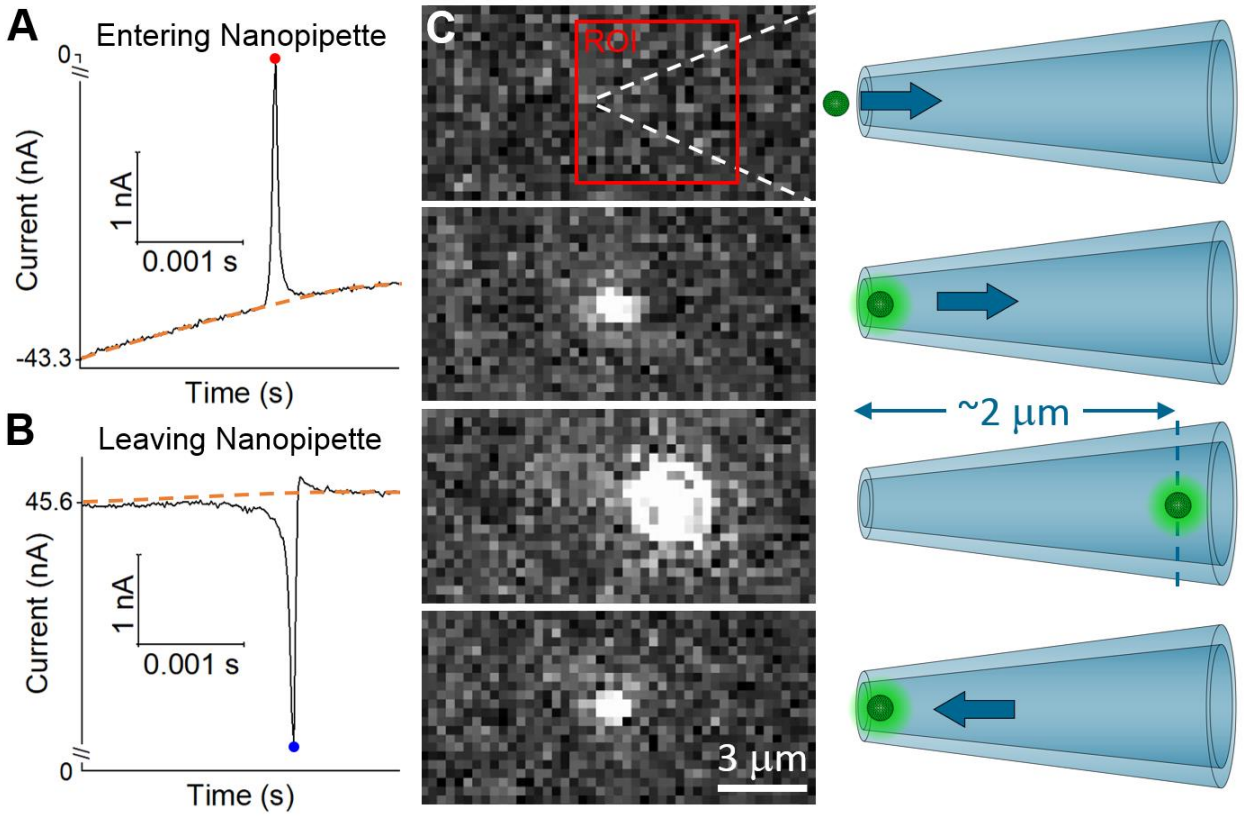

Figure 3. Example of a resistive pulse corresponding to (A) a liposome entering the nanopipette at -1.0 V, and (B) leaving the nanopipette after switching the potential to 1.0 V. The red point on (A) and blue point on (B) indicate the maximum blockage current of the resistive pulse when the liposome passes through the nanopipette orifice. The dashed orange lines show the baseline current determined with asymmetric least squares (see Supporting Information). The fluorescence images in (C) show the liposome fluorescing when inside of the nanopipette. The liposome travels ~2 µm into the nanopipette at -1.0 V and changes direction to travel out of the nanopipette when 1.0 V is applied. The approximate pipette location is shown with dashed white lines and the ROI is shown with the red box. The drawings of the liposome and the nanopipette

on the right side of the figure are not drawn to scale. A potential switching delay time of 5 ms was used. The solution contained 0.1 M NaCl, and 10 mM PB (pH 7). Nanopipette radius = 111 ± 8 nm.

The variations seen in the intensity of the fluorescence signal during liposome multipassing (Figure 2C) is hypothesized to result from three primary factors. First, the fiber illuminator emits light in a single optical mode, which can produce interference fringes within the waveguide-like nanopipette. As the liposome travels ~2–5 μm into the nanopipette (depending on the internal delay time), it traverses these interference fringes in the excitation light which produces variability in the liposome's emission intensity. In addition, vertical movement of the liposome through the objective lens depth of field, ~1 μm, and possible lensing effects from the curved nanopipette, contribute to the fluctuations in the observed fluorescence intensity (Figure S2). Lastly, the overall fluorescence emission intensity decreases as the fluorescent labels associated with the liposome slowly photobleach within the excitation light (*vide infra*).

Characterization of the fluorescence 'dead zone'. The 'on/off' fluorescence behavior observed during liposome multipassing, Figure 2C and Figure 3C, is hypothesized to result from scattering of the excitation light (488 nm) at the tip of the subwavelength nanopipette orifice (110–150 nm radius). This fluorescence 'dead zone' just outside of the nanopipette orifice was investigated by multipassing a ~100 nm radius fluorescent PS nanoparticle using longer external delay times (10 ms), enabling the particle to pass entirely through the 'dead zone' and into the external electrolyte solution where it begins to emit fluorescence again due to a portion of the excitation light traveling through the transparent glass walls of the nanopipette (Figure 1, Figure S1). Figure 4 shows a series of images during the multipassing of the ~100 nm radius fluorescent

PS nanoparticle passing through the 'dead zone'. Based on the images, the 'dead zone' extends ~1.5 μm from the tip of the nanopipette into the external solution. The observed width of the 'dead zone' was not influenced by changing the velocity of the translocating PS nanoparticle suggesting that this region originates from the geometric constraints of the subwavelength nanopipette orifice size (Figure S6). Figure S7 provides replicate experiments demonstrating the reproducibility of the 'dead zone' during multipassing of PS nanoparticles.

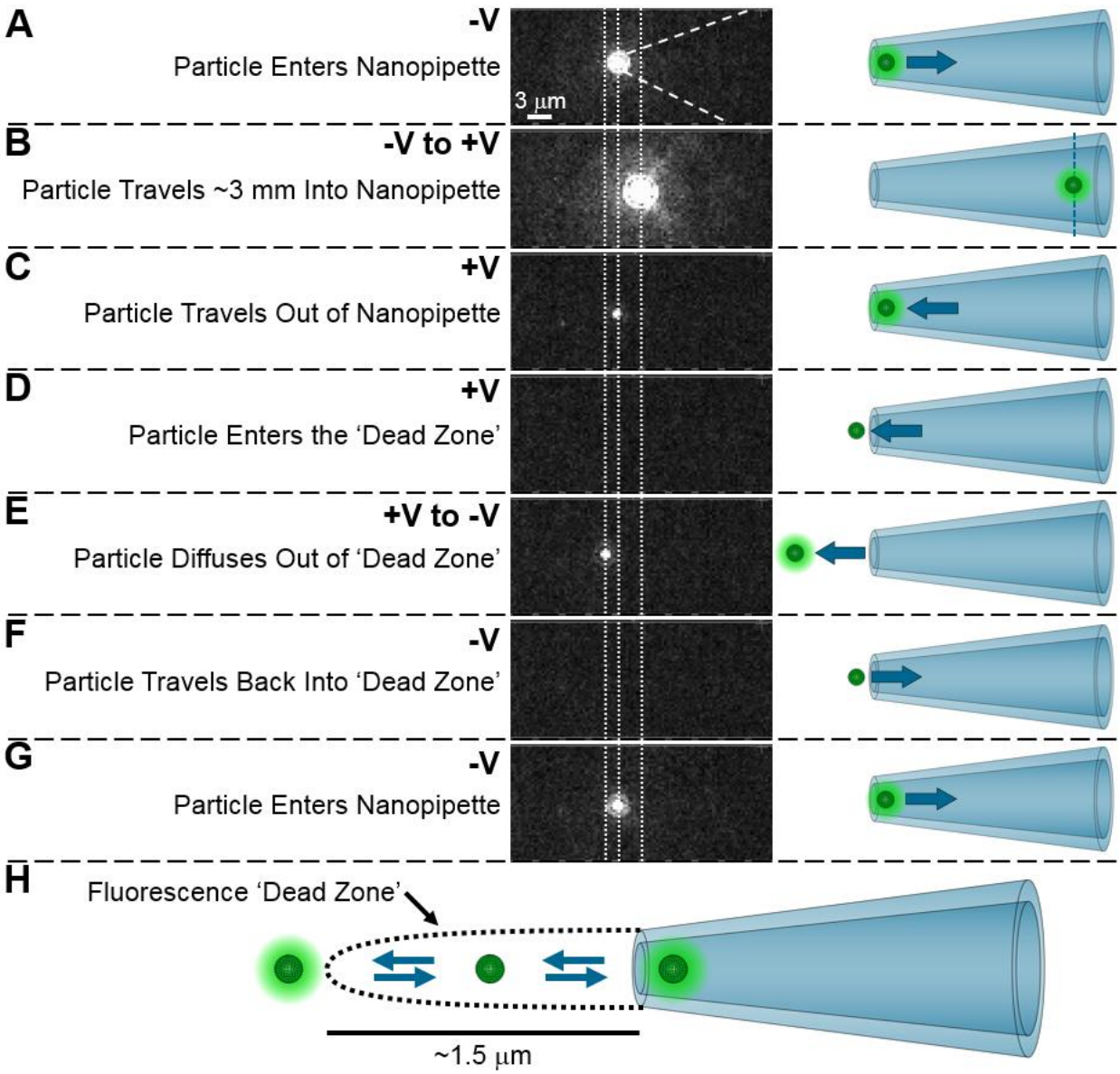

Figure 4. Sequential images of a ~100 nm radius fluorescent PS nanoparticle during multipass resistive-pulse sensing. (A) The fluorescing particle is inside of the nanopipette tip and traveling into the nanopipette at -0.5 V. The approximate location of the nanopipette is shown with dashed white lines. (B) Image of the particle after it had traveled the maximum distance into the nanopipette after an internal delay time of 10 ms. The potential is switched to 0.5 V and the particle changes direction to travel out of the nanopipette. (C) Image of particle prior to exiting the nanopipette at 0.5 V. (D) The particle immediately outside of the nanopipette orifice in the fluorescence 'dead zone' at 0.5 V. (E) The particle fluorescing in the external electrolyte solution after it had traveled ~1.5 μm away from the nanopipette tip. The potential is then switched to -0.5 V after an external delay time of 10 ms. (F) The particle travels back into the 'dead zone' towards the nanopipette. (G) The particle re-enters the nanopipette tip and fluoresces. The vertical white lines show the location of the particle when it is fluorescing in the external solution (E), just inside of the nanopipette (A, C, and G), and at the maximum distance traveled into the nanopipette (B). From these images, we estimate that the 'dead zone' extends ~1.5 μm beyond the tip of the nanopipette. (H) Diagram illustrating particle fluorescence as it passes through the fluorescence 'dead zone'. The drawings of the particle and the nanopipette on the right side of the figure are not drawn to scale. The solution contained 0.1 M NaCl, 10 mM PB pH 7, 0.1% SDS, and 0.1% Triton X-100. Nanopipette radius = 150 ± 10 nm.

Sizing liposomes with multipass resistive-pulse sensing. The radius of multipassed spherical particles can be calculated from the maximum blockage current of the resistive pulse, $\%\Delta i$, as $\%\Delta i$ is proportional to the volume of the particle.[8, 12] Eq. 1 describes the relationship between the percent blockage current and the particle radius, r, where the proportionality constant, k, is related to the orifice size of the nanopipette. The value of k was determined by

adding PS nanoparticles of known nominal radii to the liposome solution. Both the liposomes and PS nanoparticles were detected by resistive-pulse sensing and the average $\%\Delta i$ was determined for the PS particles (Figure S8).

$$\%\Delta i = kr^3 \quad (1)$$

Liposome radii are calculated from their individual $\%\Delta i$ using eq. 2.[8]

$$r_L = r_{PS,avg}\left(\frac{\%\Delta i_L}{\%\Delta i_{PS,avg}}\right)^{\frac{1}{3}} \quad (2)$$

In eq. 2, r_L is the radius of the liposome, $r_{PS,avg}$ is the average PS radius, $\%\Delta i_{PS,avg}$ is the average percent resistive pulse blockage current of the PS nanoparticles, and $\%\Delta i_L$ is the percent resistive pulse blockage current of a liposome. Use of eq. 2 assume that the liposomes are spherical and that their lipid membrane presents an infinite resistance to ion fluxes.[47] As shown in Figure S8, 90 nm radius PS nanoparticles produced an average blockage current of 1.52 ± 0.02% for a 111 ± 8 nm radius nanopipette orifice.

The uncertainty in the size of the PS nanoparticles (~5 %) used as the internal standard limits the accuracy of the resistive pulse measurement in determining the absolute value of r_L. However, the precision in determining the relative size of individual liposomes by multipassing is excellent.[8] Figure 5 demonstrates the advantage of making multiple measurements of the same liposome to achieve sub-nanometer sizing precision. In this experiment, a single liposome was multipassed 149 times through the nanopipette orifice. The ±3 SE (~99.7% confidence interval) from the moving mean of r_L shows the dramatic decrease in measurement error with increasing number of measurements. At 5 translocations, the error of the reported liposome radius is ±0.5 nm, while at 149 translocations, the radius error decreased to ±0.1 nm. A 4-fold increase in the

number of translocations (n) results in a 2-fold decrease in the error of the reported size due to the $\sqrt{n}$ relationship of SE.[8] In addition to obtaining sub-nanometer size resolution with multipassing, Figure 5 also indicates that the liposomes do not change size as they are multipassed through the nanopipette orifice. An example of multipassing a fluorescent PS nanoparticle ~5500 times, resulting in a SE of ±0.01 nm, is shown in the Supporting Information (Figure S9). Figure 5 and Figure S9 also indicate there is no significant drift in the measured current resulting from thermal fluctuations or solution evaporation during the duration of the measurement.

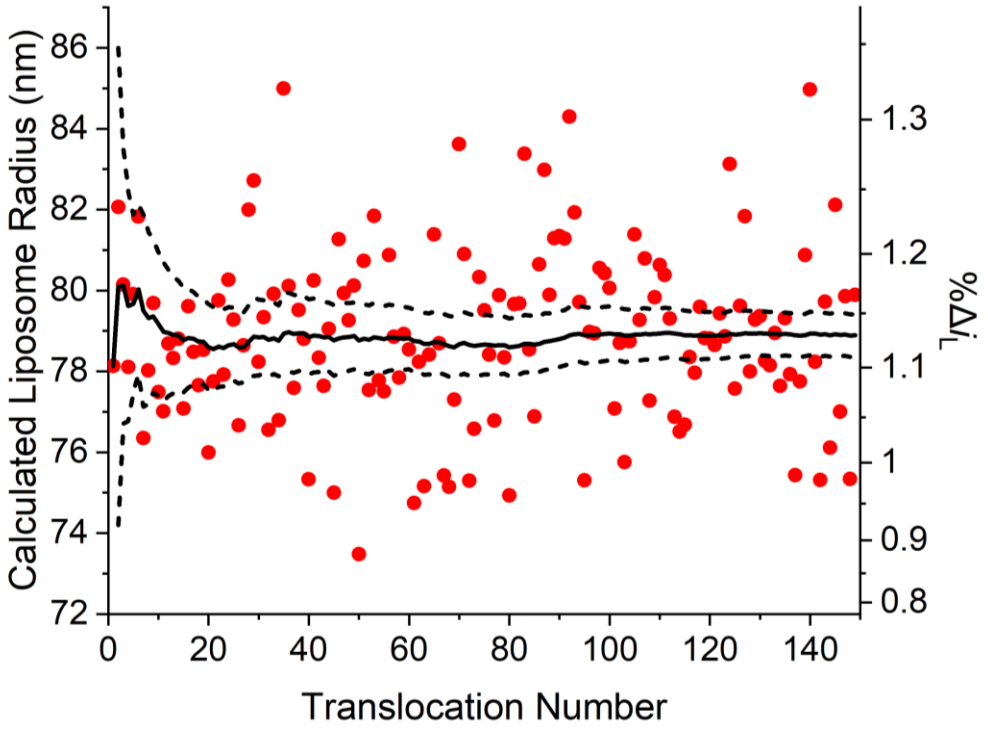

Figure 5. Calculated liposome radius and %Δi *vs.* translocation number for an individual liposome multipassed 149 times. The red points represent the calculated liposome radius and measured %Δi for each individual translocation of the liposome entering the nanopipette at -1.0 V. The black solid line represents the moving mean values of the particle radius. The dashed black lines represent ±3 SE from the mean (~99.7% confidence interval). At 149 translocations,

r_L = 53.6 ± 0.1 nm. The solution contained 0.1 M NaCl, and 10 mM PB (pH 7). Nanopipette radius = 111 ± 8 nm.

CryoTEM imaging of the *E. coli* lipid liposomes. It is expected that the liposome fluorescence intensity scales with the liposome surface area due to the presence of the membrane-bound DiO molecules. However, it was observed that a sub-population of liposomes produced greater fluorescence signals than others of similar radii (*vide infra*). We hypothesized that these differences in the fluorescence intensity results from varying degrees of liposome lamellarity. The fluorescent DiO molecules are present in all membrane surfaces of the liposome, including internal membranes of multi-vesicle liposomes. Liposomes with increased degrees of lamellarity are predicted to have an increased fluorescence signal due to an increase in the total membrane surface area. To validate this hypothesis, we performed CryoTEM imaging to determine the distribution of liposome lamellarity as well as the size distribution of the liposome sample.

Unilamellar liposomes and multi-vesicle liposomes with either one internal liposome (MV-1) or two internal liposomes (MV-2) were observed in the sample. Example cryoTEM images of the respective liposome types are shown in Figure 6A–C. Additional cryoTEM images are shown in Figure S10. The analysis of the cryoTEM images indicate that 87% are unilamellar, 12% are MV–1, and 1% are MV–2 (N_{total} = 2839, Figure S11). The liposomes were also sized with dynamic light scattering (DLS) (Figure S12). A comparison of the sizing methods is shown in Figure S13 and show agreement between the two methods, $r_{cryoTEM}$ = 39 ± 15 nm and r_{DLS} = 45 ± 15 nm (here, the reported error is the standard deviation of the distribution of the radii). As expected, the average radii determined with DLS is slightly larger than the radii determined with cryoTEM imaging due to the weak weighting of smaller particles in the DLS measurements.[45, 49]

Due to a limited signal to noise (S/N) ratio of resistive-pulse sensing using a 111 nm radius pipette, only liposomes with radii greater than ~50 nm produced quantifiable resistive pulses (Figure S13). Liposomes with radii <50 nm produced resistive pulses too small to detect over the signal noise. For liposomes that were larger than 50 nm in radius, the cryoTEM images indicated that 72% are unilamellar, 27% are MV−1, and 1% are MV−2 (N_{total} =406). There is a slight increase in the degree of lamellarity in larger liposomes.

Figure 6D shows a plot of the total membrane surface area of the liposomes (including the membrane surface areas of the internal liposomes of multi-vesicle liposomes) *vs.* the outer surface area of liposomes with radii >50 nm. The total membrane surface areas were determined from the cryoTEM images, which include the surface areas of both sides of the phospholipid membrane assuming a membrane thickness of 4.1 ± 0.3 nm.[48] As expected, the unilamellar liposomes exhibit a linear relationship in the plot of total membrane surface area *vs.* the outer surface area of the liposome, while the multi-vesicle liposomes exhibit variations in this relationship due to a distribution of sizes of the internal liposome(s) (Figure S11). The distribution of liposome lamellarity shown in Figure 6D can be used to predict the lamellarity of a liposome characterized with resistive-pulse sensing.

It was observed that some multipassed liposomes shown in Figure 6E produced a higher fluorescence response compared to other liposomes of similar size. We attribute these differences in fluorescence intensity to the different lamellarity structures of the liposomes. Multi-vesicle liposomes will produce a greater fluorescence intensity compared to unilamellar liposomes due to additional DiO molecules located in the membrane(s) of the internal liposome(s) of multi-vesicle liposomes. Figure 6E shows the plot of the average fluorescence intensity *vs.* the outer surface area of the liposome for liposomes that were multipassed 5 times.

The surface area of the liposome was calculated from r_L determined by resistive-pulse sensing. As expected, the magnitude of the fluorescence response increases with increasing liposome surface area.

The lamellarity distribution of liposomes characterized with multipass resistive-pulse sensing and fluorescence imaging is well approximated by the lamellarity distribution obtained from the cryoTEM imaging and shown in Figure 6D. Thus, we assign the data points within the green-shaded region of Figure 6E to unilamellar liposomes and the data points within the blue-shaded region to multi-vesicle liposomes. The assignment of liposome lamellarity in the resistive pulse studies is only approximate due to photobleaching and the error in the fluorescence signal.

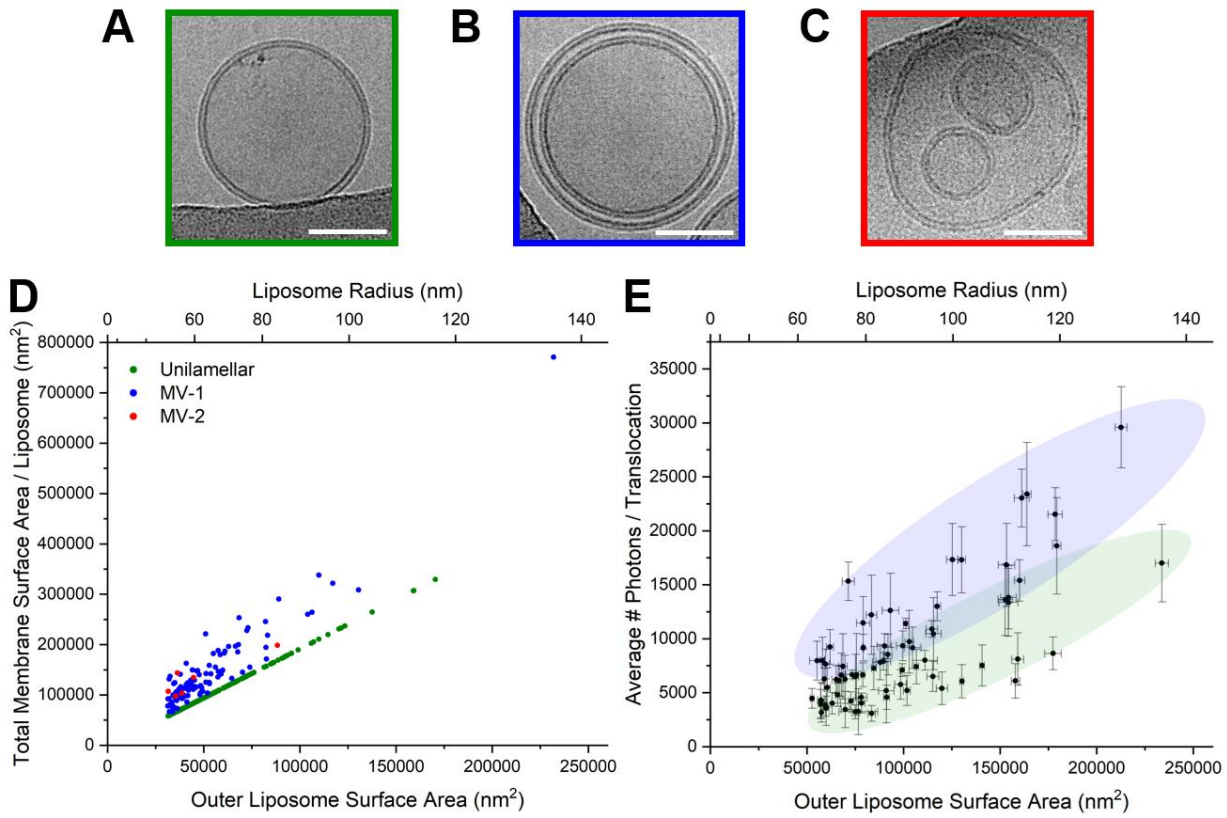

Figure 6. CryoTEM analysis of DiO-labeled *E. coli* lipid liposomes. Example images of (A) a unilamellar liposome, (B) a MV−1 liposome, and (C) a MV−2 liposome. Scale bars = 50 nm. (D)

Total membrane surface area of all lamellar structures within a liposome *vs.* the outer surface area of the liposome and liposome radius. The total membrane surface area was calculated from the liposome radii measured in the cryoTEM images and includes the surface area of both sides of the phospholipid membrane(s) assuming a membrane thickness of 4.1 ± 0.3 nm.[48] 406 liposomes with radii >50 nm were analyzed. The green points correspond to unilamellar liposomes, blue correspond to MV−1 liposomes, and red corresponds to MV−2 liposomes. (E) Average number of photons per translocation *vs.* the outer surface area of the liposome for 74 individual liposomes characterized with resistive-pulse sensing. The surface area of the liposome exterior was calculated using r_L from 5 liposome multipasses. Based on the liposome lamellarity distribution observed in (D), the green shading corresponds to unilamellar liposomes while the blue shading corresponds to multi-vesicle liposomes. This lamellarity assignment in (E) is only approximate. The percent distribution obtained from the cryoTEM images of unilamellar and multi-vesicle liposomes with radii >50 nm was considered in the assignment.

High-throughput liposome characterization. Multipass resistive-pulse sensing has been previously established as a high-throughput technique to characterize nanoparticles.[8] The frequency of particle capture is dependent on the particle concentration in the external solution.[8] At the concentration of liposomes used in this study, ~5×10^9 liposomes/mL, a new liposome is characterized approximately every second. The capture of a new liposome follows the loss of the previous liposome, which occurs after a liposome has diffused too far away from the nanopipette orifice to be recaptured. In this study, the complete data set details ~350 liposomes characterized with multipass resistive-pulse sensing and fluorescence imaging in 400 s (data not shown). Figure 8 shows an example section of the data where 8 different liposomes were multipassed in

~8 seconds demonstrating our ability to rapidly characterize the size and fluorescence signal of fluorescent liposomes. The radii of liposomes shown in Figure 8A were calculated from the resistive pulses shown in Figure 8B using eq. 2.

Liposomes undergo photobleaching during multipassing, which can be seen in the fluorescence-time trace shown in Figure 8C, where the photobleaching trend follows an exponential decay.[49, 50] Multipassed liposomes are identified based on the magnitude of the resistive pulses, but can also be identified based on the decay of their fluorescence signal. Recaptured photobleached liposomes display a response identical to a non-fluorescent (photobleached) liposome. Partial photobleaching of particles is also possible. When a partially photobleached particle is recaptured, the fluorescence intensity resumes the photobleaching trend where it left off in the previous multipassing (Figure S14). Additionally, since the fluorescence response is approximately proportional to the particle size, it is possible to estimate r_L from the fluorescence alone. An example of multipassing 100 nm and 50 nm nominal radius fluorescent PS nanoparticles in the same solution can be found in the Supporting Information that further demonstrates the correlation between particle size and fluorescence intensity (Figure S15). In future work, we plan to implement anti-fading agents (*e.g.*, triplet state quenchers, oxygen scavenging systems) which have been shown to significantly increase photostability.[51-53]

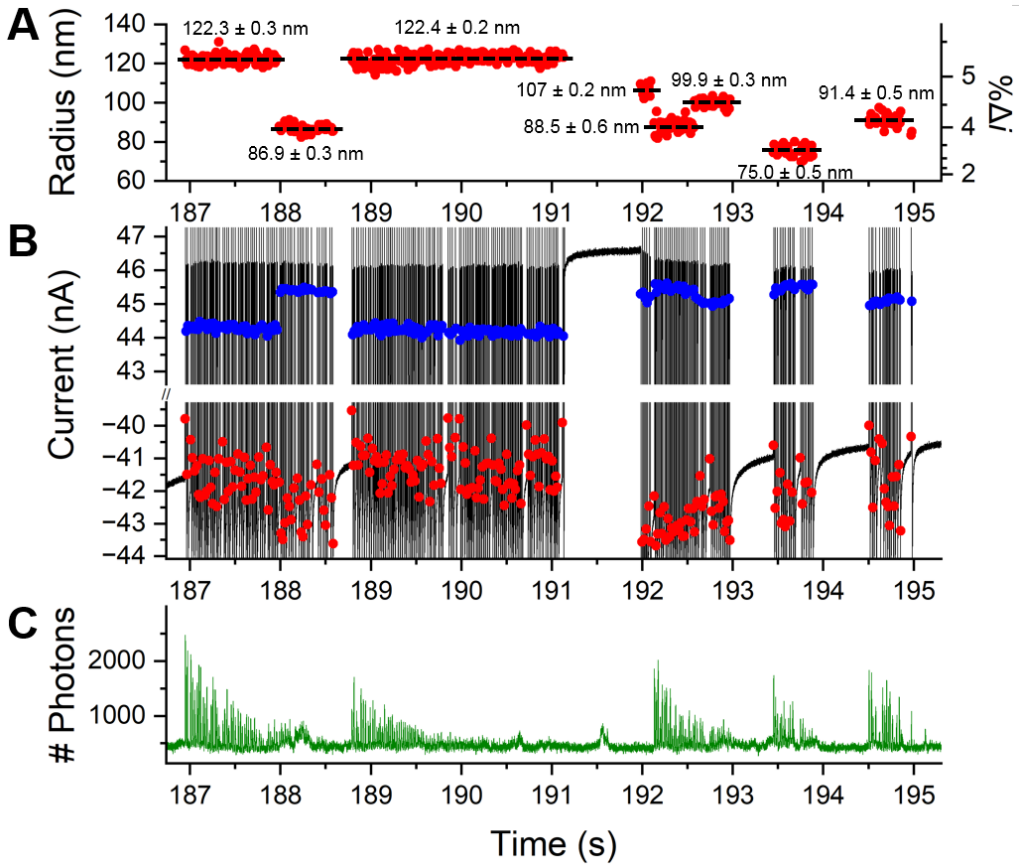

Figure 8. Eight different liposomes with radii ranging from 75 ± 0.5 nm to 122.4 ± 0.2 nm were multipassed using ±1.0 V and simultaneously imaged to record liposome fluorescence. (A) The calculated liposome radii based on resistive pulses associated with liposomes entering the nanopipette at -1.0 V. (B) The *i-t* trace of the liposome resistive pulses, where the red points are associated with the liposome entering the nanopipette at -1.0 V and the blue points in (B) are associated with the liposomes leaving the nanopipette at 1.0 V. (C) Fluorescence *vs.* time trace that was recorded simultaneously during liposome multipassing. Photobleaching of the liposomes is observed in (C) as indicated by the exponential decrease in fluorescence intensity during the multipassing of the individual liposomes. Potential switching delay times of 5 ms were used. The solution contained 0.1 M NaCl, and 10 mM PB (pH 7). Nanopipette radius = 111 ± 8 nm.

Characterization of fluorescent and non-fluorescent liposomes. A significant advantage of simultaneous multipass resistive-pulse sensing and fluorescence imaging is the ability to distinguish between liposomes with and without fluorescent markers. For example, Figure 9 shows the simultaneous characterization of a completely photobleached, non-fluorescent liposome and a fluorescent liposome. This smaller, 70.3 ± 0.7 nm, liposome is non-fluorescent due to prolonged exposure to the excitation light inside of the nanopipette, resulting in complete photobleaching. This liposome originated from the inside of the nanopipette as indicated by its first resistive pulse corresponding to a particle leaving the nanopipette orifice at 1.0 V (Figure 8A). The second, larger, 95.4 ± 0.3 nm, fluorescent liposome originated from the external electrolyte solution (its first resistive pulse corresponds to a particle entering the nanopipette orifice at -1.0 V) has not been photobleached in the interior of the nanopipette and exhibits typical liposome fluorescence. Additional examples of particle photobleaching can be found in the Supporting Information (Figure S16–S17). The qualitative detection of particle fluorescence will be useful in future studies of biologically relevant particles to probe specific surface markers with fluorescent labeling.

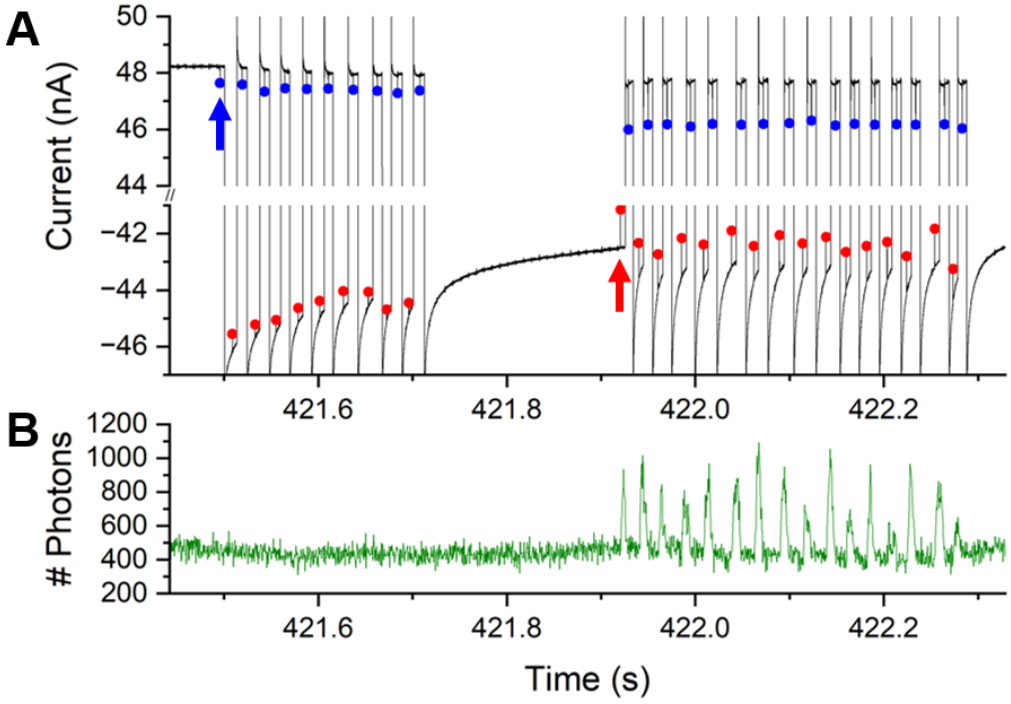

Figure 9. Multipassing of a non-fluorescent 70.3 ± 0.7 nm liposome (left) and a 95.4 ± 0.3 nm fluorescent liposome (right) at ±1.0 V. (A) The *i-t* trace including resistive pulses of the non-fluorescent and fluorescent liposome. The blue points in (A) correspond to the liposomes leaving the nanopipette at 1.0 V and the red points correspond to the liposomes entering the nanopipette at -1.0 V. The non-fluorescent liposome originated from inside of the nanopipette, as indicated by its first resistive pulse at 1.0 V (blue arrow), and the fluorescent liposome originated from the external solution, as indicated by its first resistive pulse at -1.0 V (red arrow). (B) The corresponding fluorescence-time trace recorded simultaneously with the *i-t* trace. Potential switching delay times of 5 ms were used. The solution contained 0.1 M NaCl, and 10 mM PB (pH 7). Nanopipette radius = 111 ± 8 nm.

CONCLUSIONS

In conclusion, we have demonstrated the capability to measure the size and fluorescence signal of individual DiO-labeled *E. coli* lipid liposomes and distinguish between fluorescent and non-fluorescent liposomes using simultaneous multipass resistive-pulse sensing and fluorescence imaging. DiO-labeled *E. coli* lipid liposomes were used as a model system to represent biologically relevant nanoparticles. Three types of liposomes (unilamellar and multi-vesicle liposomes with one internal liposome and two internal liposomes) were identified in our sample using cryoTEM imaging. The distribution of liposome lamellarity obtained from the cryoTEM images was used to predict the lamellarity of liposomes analyzed with simultaneous resistive-pulse sensing and fluorescence imaging. The assignment of lamellarity based on liposome fluorescence intensity and resistive-pulse measured radius was in general agreement with the distribution of lamellarity observed from the cryoTEM images. A fluorescence 'dead zone' located external to the nanopipette orifice was observed that resulted in an 'on/off' fluorescent behavior during liposome multipassing. This fluorescence exclusion zone originates from the excitation light being unable to propagate through the subwavelength orifice of the nanopipette, resulting in liposomes only emitting fluorescence when located inside of the nanopipette during multipassing.

To summarize, multipass resistive-pulse sensing combined with fluorescence imaging enables the characterization of *individual* biologically relevant particles with sub-nanometer sizing precision and fluorescent labeling. Studying the contents of specific sub-populations of cancer-derived EVs is critical to a fundamental understanding of the disease, and there remains an urgent need to characterize EVs on an individual basis to understand the relationship between EV size, surface properties, and contents. Future applications of the methodology described here

aim to profile the relationship between the sizes of extracellular vesicles (EVs) of cancerous origin and targeted surface proteins using resistive-pulse sensing and fluorescent labeling.

METHODS

Chemicals

Sodium chloride, sodium phosphate dibasic heptahydrate, sodium phosphate monobasic monohydrate, 200-proof ethanol, sodium dodecyl sulfate (SDS), and Triton X-100 was obtained from Thermo Fisher Scientific and used without further purification. Water (18.2 MΩ·cm) was obtained from a Thermo Scientific Barnstead Smart2Pure water system. *E. coli* polar lipid extract was purchased from Avanti Polar Lipids (Alabaster, AL) and stored at -80 °C until use. 3, 3-dioctadecyloxacarbocyanine (DiO) was purchased from Biotium and stored at 4^{o} C in the dark. Fluorescent polystyrene nanoparticles were purchased from ThermoFisher (FluoSpheres™ Carboxylate-modified Microspheres, $\lambda_{em} \geq 515$ nm) and stored at 4^{o} C in the dark.

Preparation of Liposomes

A standard extrusion technique was used to create DiO-labeled *E. coli* lipid liposomes. Briefly, *E. coli* polar lipid extract was dissolved in chloroform to a concentration of 0.10 mg/100 μL. DiO was dissolved in chloroform to a concentration of 1.0 mg/400 μL. Aliquots of 400 μL (0.40 mg) of the *E. coli* lipid solution and 18.4 μL (45.9 μg) of the DiO solution were combined in a 50 mL round bottom flask and the chloroform was evaporated off under an N_2 stream until visibly dry. The round bottom flask was kept in the dark to limit the exposure of the DiO dye to light. Trace amounts of chloroform was removed by further drying the lipid-DiO mixture under

vacuum (95 mbar) for 2 hours at room temperature. Lipid containing DiO was rehydrated at room temperature in 1 mL of 0.1 M NaCl and 10 mM phosphate buffer (PB) at pH 7. The lipid solution was gently mixed and then vortexed for ~1 minute and left to sit for 30 minutes to rehydrate. Liposomes were formed by extrusion with an Avanti Mini Extruder using a 100 nm extrusion membrane (Avanti Polar Lipids) and were passed through the membrane 51 times. Liposomes were used on the same day they were extruded. The concentration of liposomes used in the multipass studies is ~5×10^9 mL^{-1}, assuming complete conversion from the lipid solution to liposomes.

The liposomes were sized using three different methods (1) an internal standard of PS nanoparticles with known radii (Figure S8), (2) cryoTEM imaging (Titan Krios G3 cryo Transmission Electron Microscope, Thermo Fisher Scientific) using 1.2/1.3 and 2/1 holey carbon grids (Quantifoil) (Figure S10), and (3) number-weighted dynamic light scattering (DLS) with a NiComp 380 ZLS ζ potential analyzer (Particle Sizing Systems) (Figure S12). The liposome lamellarity was determined with cryoTEM imaging (Figure S12).

Nanopipette Fabrication

Pulled glass nanopipettes were fabricated using a P-2000 laser puller (Sutter Instruments). Quartz capillaries (1.0 mm outer diameter, 0.7 mm inner diameter, Sutter Instruments) were pulled using a single line program with the following parameters: heat: 560 filament: 3, velocity: 30, delay: 145, pull: 175. The orifice of the nanopipettes were sized by measuring the pressure to extrude bubbles from the pipette tip in 200-proof ethanol.[54] Pipettes were backfilled using a Microfil syringe tip (MF28G, World Precision Instruments) with 0.1 M NaCl and 10 mM PB (pH 7).

Resistive Pulse Measurements with Simultaneous Fluorescence Imaging

The experimental cell shown in Figure 1 and Figure S1 was fit onto the stage of an inverted microscope (IX50, Olympus) and filled with the external aqueous electrolyte solution (0.1 M NaCl and 10 mM PB, pH 7 for liposome studies and 0.1 M NaCl, 10 mM PB (pH 7), 0.1% SDS, and 0.1 % Triton X-100 for PS studies). The SDS and Triton X-100 surfactants were needed to prevent the PS particles from irreversibly adsorbing onto the nanopipette surface. The nanopipette was filled with the same electrolyte as the external electrolyte solution. The internal Ag/AgCl electrode and fiber optic cable (405-532nm Single Mode Patch Cable, Thorlabs) was inserted into the back of the nanopipette using a SMA Opto-pipette holder attached to a SMA dovetail fiber holder (HEKA Elektronik). The optical fiber was positioned ~ 1 mm from the end of the nanopipettes tip. The pipette holder was attached to a micromanupliator (MP-225, Sutter Instruments) and positioned over the microscope objective (LCPlanFl 40x/0.60 na, Olympus). A fiber coupled laser source (Agiltron) was used to deliver the 488 nm excitation light at 2 mW power through the fiber optic. A 500 nm high-pass emission filter was used in the inverted microscope to block light below 500 nm, including the 488 nm excitation light, from reaching the detector. The entire experimental setup was placed inside of a large grounded Faraday cage. The nanopipette was submerged in the external electrolyte solution at a 45^{o} angle with the nanopipette tip in focus of the optical objective (Figure 1). A second Ag/AgCl electrode was placed in the external electrolyte solution. Fluorescent liposomes or fluorescent PS nanoparticles were added to the external electrolyte solution at a concentration of ~5×10^{9} particles per mL. The voltage was applied to the external Ag/AgCl electrode relative to the internal Ag/AgCl electrode. The current was recorded using an AC/DC capable Nanopatch system (Electronic BioSciences, Salt Lake City, Utah). The analog to digital conversion is performed by a Kintex-7

FPGA on a National Instruments PCIe-7857 data acquisition card. The FPGA is programmed to acquire, filter, and down-sample the current data. After appropriate thresholds are set, the FPGA performs threshold detection to detect the passage of a particle through the nanopipette and quickly switch the bias voltage to reverse the direction of the particle motion. The current data is then streamed to the host computer to be displayed and saved. Current-time data were recorded at 50 kHz with a 10 kHz LPF.

The fluorescence images were recorded using an Andor Zyla sCMOS camera from Andor Oxford Instruments using the Andor Solis software. Videos were sampled at 2000 frames per second with an image dimension of 45 × 200 pixels. The analogue-to-digital-units (ADU) fluorescence intensity was converted to the number of photons by calibrating the camera detector gain from a series of gradient images (Figure S4).[43]

Data Processing

The percent blockage current of each resistive pulse was calculated as the height of resistive pulse blockage relative to the baseline current (Figure S5). The baseline current of the *i*-*t* trace was fit using asymmetric least squares to determine the baseline current at the time of the resistive pulse (See Supporting Information and Figure S5).[8]

The fluorescence images (40 × 200 pixels) were cropped into a smaller region of interest (ROI) of (18 × 18 pixels) located at the tip of the nanopipette to quantify the fluorescence signal as the liposomes and PS particles moved through sensing region (Figure S3).

The *i*-*t* traces and fluorescence-time traces were aligned to within 0.5 ms using cross-correlation time alignment methods.[17] The time at which liposomes entered the nanopipette was

cross-correlated with the time associated with the onset of the fluorescence signal during the liposome multipassing to perform the alignment.

AUTHOR INFORMATION

Corresponding Authors

Henry S. White − Department of Chemistry, University of Utah, Salt Lake City, Utah 84112, United States; https://orcid.org/0000-0002-5053-0996

Sean R. German – Electronic BioSciences, Inc., 421 Wakara Way, Suite 328, Salt Lake City, Utah 84108, United States; https://orcid.org/0000-0002-4636-4577

Authors

Alexandra J. Schmeltzer − Department of Chemistry, University of Utah, Salt Lake City, Utah 84112, United States; https://orcid.org/0000-0003-1873-2413

Eric M. Peterson – Electronic BioSciences, Inc., 421 Wakara Way, Suite 328, Salt Lake City, Utah 84108, United States; https://orcid.org/0000-0001-6694-589X

Daniel K. Lathrop – Electronic BioSciences, Inc., 421 Wakara Way, Suite 328, Salt Lake City, Utah 84108, United States; https://orcid.org/0009-0002-8033-1901

Conflict of Interest

The authors declare the following competing financial interest: S.R.G., E.M.P., and D.K.L. are employees of Electronic BioSciences, Inc.

ACKNOWLEDGEMENTS

We would like to thank Prof. Joel M. Harris for helpful discussions regarding the assignment of liposome lamellarity in the multipass resistive pulse studies of the fluorescent liposomes. CryoTEM imaging of *E. coli* lipid liposomes was performed by Dr. Barbie K. Ganser-Pornillos at the University of Utah Electron Microscopy Core Laboratory. This work was supported by the National Institutes of Health (R41CA265607).

SUPPORTING INFORMATION AVAILABLE

Video of a multipassing fluorescent liposome, pictures of the experimental setup, distance particles travel into the nanopipette as a function of potential switching delay time, fluorescence image region of interest, camera calibration for converting ADU to number of photons, code for asymmetric least squares analysis of baseline currents, measuring the resistive pulse blockage currents, fluorescence dead zone *vs.* applied potential and reproducibility of the fluorescence dead zone, sizing liposomes with an internal standard, multipassing a PS nanoparticle 5500 times, cryoTEM images of DiO-labeled *E. coli* lipid liposomes, sizing liposomes with dynamic light scattering, comparison of liposome sizing methods, recapturing nanoparticles during multipassing, multipassing fluorescent PS nanoparticles, photobleaching of multipassing nanoparticles.

REFERENCS

1. Zaborowski, M. P.; Balaj, L.; Breakefield, X. O.; Lai, C. P. Extracellular Vesicles: Composition, Biological Relevance, and Methods of Study. *Bioscience* **2015**, *65*, 783-797.
2. Aharon, A.; Rebibo-Sabbah, A.; Ahmad, R. S.; Dangot, A.; Bar-Lev, T. H.; Brenner, B.; Cohen, A. H.; David, C. B.; Weiner, Z.; Solt, I. Associations of Maternal and Placental Extracellular Vesicle miRNA with Preeclampsia. *Front Cell Dev Biol* **2023**, *11*, 1080419.
3. Zhang, H. Y.; Freitas, D.; Kim, H. S.; Fabijanic, K.; Li, Z.; Chen, H. Y.; Mark, M. T.; Molina, H.; Martin, A. B.; Bojmar, L.; Fang, J.; Rampersaud, S.; Hoshino, A.; Matei, I.;

Kenific, C. M.; Nakajima, M.; Mutvei, A. P.; Sansone, P.; Buehring, W.; Wang, H. J. *et al.* Identification of Distinct Nanoparticles and Subsets of Extracellular Vesicles by Asymmetric Flow Field-Flow Fractionation. *Nat Cell Biol* **2018**, *20*, 332-343.
4. Mendivil-Alvarado, H.; Sosa-Leon, L. A.; Carvajal-Millan, E.; Astiazaran-Garcia, H. Malnutrition and Biomarkers: A Journey through Extracellular Vesicles. *Nutrients* **2022**, *14*, 1002.
5. Berge, L. I.; Feder, J.; Jossang, T. Single-Particle Flow Dynamics in Small Pores by the Resistive Pulse and the Pressure Reversal Technique. *J. Colloid Interface Sci.* **1990**, *138*, 480-488.
6. Deblois, R. W.; Bean, C. P. Counting and Sizing of Submicron Particles by Resistive Pulse Technique. *Rev. Sci. Instrum.* **1970**, *41*, 909-916.
7. Deblois, R. W.; Bean, C. P.; Wesley, R. K. A. Electrokinetic Measurements with Submicron Particles and Pores by Resistive Pulse Technique. *J. Colloid Interface Sci.* **1977**, *61*, 323-335.
8. Edwards, M. A.; German, S. R.; Dick, J. E.; Bard, A. J.; White, H. S. High-Speed Multipass Coulter Counter with Ultrahigh Resolution. *ACS Nano* **2015**, *9*, 12274-12282.
9. German, S. R.; Luo, L.; White, H. S.; Mega, T. L. Controlling Nanoparticle Dynamics in Conical Nanopores. *J. Phys. Chem. C* **2013**, *117*, 703-711.
10. Golibersuch, D. C. Observation of Aspherical Particle Rotation in Poiseuille Flow Via Resistance Pulse Technique .2. Application to Fused Sphere Dumbbells. *J. Appl. Phys.* **1973**, *44*, 2580-2584.
11. Harms, Z. D.; Mogensen, K. B.; Nunes, P. S.; Zhou, K. M.; Hildenbrand, B. W.; Mitra, I.; Tan, Z. N.; Zlotnick, A.; Kutter, J. P.; Jacobson, S. C. Nanofluidic Devices with Two Pores in Series for Resistive-Pulse Sensing of Single Virus Capsids. *Anal. Chem.* **2011**, *83*, 9573-9578.
12. Ito, T.; Sun, L.; Crooks, R. M. Simultaneous Determination of the Size and Surface Charge of Individual Nanoparticles Using a Carbon Nanotube-based Coulter Counter. *Anal. Chem.* **2003**, *75*, 2399-2406.
13. Kozak, D.; Anderson, W.; Vogel, R.; Chen, S.; Antaw, F.; Trau, M. Simultaneous Size and Zeta-Potential Measurements of Individual Nanoparticles in Dispersion Using Size-Tunable Pore Sensors. *ACS Nano* **2012**, *6*, 6990-6997.
14. Lan, W. J.; Holden, D. A.; Zhang, B.; White, H. S. Nanoparticle Transport in Conical-Shaped Nanopores. *Anal. Chem.* **2011**, *83*, 3840-3847.
15. Qin, Z. P.; Zhe, J. A.; Wang, G. X. Effects of Particle's Off-axis Position, Shape, Orientation and Entry Position on Resistance Changes of Micro Coulter Counting Devices. *Meas. Sci. Technol.* **2011**, *22*, 045804.
16. Qiu, Y. H.; Hinkle, P.; Yang, C.; Bakker, H. E.; Schiel, M.; Wang, H.; Melnikov, D.; Gracheva, M.; Toimil-Molares, M. E.; Imhof, A.; Siwy, Z. S. Pores with Longitudinal Irregularities Distinguish Objects by Shape. *ACS Nano* **2015**, *9*, 4390-4397.
17. Souza, G. P. D.; Boaventura, W. D. Time-alignment of Electrical Network Measurements Through Time Series of Cycle RMS Values. *Int J Elec Power* **2023**, *144*, 108518.
18. Vogel, R.; Willmott, G.; Kozak, D.; Roberts, G. S.; Anderson, W.; Groenewegen, L.; Glossop, B.; Barnett, A.; Turner, A.; Trau, M. Quantitative Sizing of Nano/Microparticles with a Tunable Elastomeric Pore Sensor. *Anal. Chem.* **2011**, *83*, 3499-3506.

19. German, S. R.; Hurd, T. S.; White, H. S.; Mega, T. L. Sizing Individual Au Nanoparticles in Solution with Sub-Nanometer Resolution. *ACS Nano* **2015**, *9*, 7186-7194.
20. Coulter, W. H. Means for Counting Particles Suspended in a Fluid. US 2656508A, October 20, 1953.
21. Coulter, W. H. High Speed Automatic Blood Cell Counter and Cell Size Analyzer. *Proc. of the National Electron Conference* **1956**, *12*, 1034-1042.
22. Graham, M. D. The Coulter Principle: A History. *Cytometry. Part A : the journal of the International Society for Analytical Cytology* **2022**, *101*, 8-11.
23. Yan, J. S.; Wang, C.; Fu, Y. S.; Guo, J. C.; Guo, J. H. 3D Printed Microfluidic Coulter Counter for Blood Cell Analysis. *Analyst* **2022**, *147*, 3225-3233.
24. Wang, Y. L.; Chen, D. N.; Guo, X. L. Cell Density Detection Based on a Microfluidic Chip with Two Electrode Pairs. *Biotechnol. Lett* **2022**, *44*, 1301-1311.
25. Bilican, I.; Guler, M. T.; Serhatlioglu, M.; Kirindi, T.; Elbuken, C. Focusing-Free Impedimetric Differentiation of Red Blood Cells and Leukemia Cells: A System Optimization. *Sensor Actuat B-Chem* **2020**, *307*, 127531.
26. Yi, Q. L.; Cui, J.; Xiao, M.; Tang, M. Z.; Zhang, H. C.; Zhang, G.; Yang, W. H.; Xu, Y. C. Rapid Phenotypic Antimicrobial Susceptibility Testing Using a Coulter Counter and Proliferation Rate Discrepancy. *Acs Omega* **2023**, *8*, 16298-16305.
27. Kim, J. S.; Kwon, S. Y.; Lee, J. Y.; Kim, S. D.; Kim, D. Y.; Kim, H.; Jang, N.; Wang, J. J.; Han, M.; Kong, S. H. High-Throughput Multi-Gate Microfluidic Resistive Pulse Sensing for Biological Nanoparticle Detection. *Lab Chip* **2023**, *23*, 1945-1953.
28. Pan, R. R.; Hu, K. K.; Jia, R.; Rotenberg, S. A.; Jiang, D. C.; Mirkin, M. V. Resistive-Pulse Sensing Inside Single Living Cells. *J. Am. Chem. Soc.* **2020**, *142*, 5778-5784.
29. Pan, R. R.; Hu, K. K.; Jiang, D. C.; Samurai, U.; Mirkin, M. V. Electrochemical Resistive-pulse Sensing. *J. Am. Chem. Soc.* **2019**, *141*, 19555-19559.
30. Barlow, S. T.; Zhang, B. Fast Detection of Single Liposomes Using a Combined Nanopore Microelectrode Sensor. *Anal. Chem.* **2020**, *92*, 11318-11324.
31. Holden, D. A.; Watkins, J. J.; White, H. S. Resistive-Pulse Detection of Multilamellar Liposomes. *Langmuir* **2012**, *28*, 7572-7577.
32. Darvish, A.; Lee, J. S.; Peng, B.; Saharia, J.; VenkatKalyana Sundaram, R.; Goyal, G.; Bandara, N.; Ahn, C. W.; Kim, J.; Dutta, P.; Chaiken, I.; Kim, M. J. Mechanical characterization of HIV-1 with a solid-state nanopore sensor. *Electrophoresis* **2019**, *40*, 776-783.
33. Gershow, M.; Golovchenko, J. A. Recapturing and Trapping Single Molecules with a Solid-state Nanopore. *Nat Nanotechnol* **2007**, *2*, 775-779.
34. Harrell, C. C.; Choi, Y.; Horne, L. P.; Baker, L. A.; Siwy, Z. S.; Martin, C. R. Resistive-pulse DNA detection with a conical nanopore sensor. *Langmuir* **2006**, *22*, 10837-10843.
35. Zhang, Y. L.; Edwards, M. A.; German, S. R.; White, H. S. Multipass Resistive-Pulse Observations of the Rotational Tumbling of Individual Nanorods. *J. Phys. Chem. C* **2016**, *120*, 20781-20788.
36. Tkach, M.; Thalmensi, J.; Timperi, E.; Gueguen, P.; Nevo, N.; Grisard, E.; Sirven, P.; Cocozza, F.; Gouronnec, A.; Martin-Jaular, L.; Jouve, M.; Delisle, F.; Manel, N.; Rookhuizen, D. C.; Guerin, C. L.; Soumelis, V.; Romano, E.; Segura, E.; Thery, C. Extracellular vesicles from triple negative breast cancer promote pro-inflammatory macrophages associated with better clinical outcome. *Proc. Natl. Acad. Sci. U. S. A.* **2022**, *119*, e2107394119.

37. Ito, T.; Sun, L.; Crooks, R. M. Observation of DNA Transport Through a Single Carbon Nanotube Channel Using Fluorescence Microscopy. *Chem. Commun.* **2003**, 1482-1483.
38. McNally, B.; Singer, A.; Yu, Z. L.; Sun, Y. J.; Weng, Z. P.; Meller, A. Optical Recognition of Converted DNA Nucleotides for Single-Molecule DNA Sequencing Using Nanopore Arrays. *Nano Lett.* **2010**, *10*, 2237-2244.
39. Soni, G. V.; Singer, A.; Yu, Z. L.; Sun, Y. J.; McNally, B.; Meller, A. Synchronous Optical and Electrical Detection of Biomolecules Traversing Through Solid-state Nanopores. *Rev. Sci. Instrum.* **2010**, *81*, 014301.
40. Han, C.; Hao, R.; Fan, Y. S.; Edwards, M. A.; Gao, H. F.; Zhang, B. Observing Transient Bipolar Electrochemical Coupling on Single Nanoparticles Translocating through a Nanopore. *Langmuir* **2019**, *35*, 7180-7190.
41. Hauer, P.; Le Ru, E. C.; Willmott, G. R. Co-ordinated Detection of Microparticles Using Tunable Resistive Pulse Sensing and Fluorescence Spectroscopy. *Biomicrofluidics* **2015**, *9*, 014110.
42. Yu, Y.; Sundaresan, V.; Bandyopadhyay, S.; Zhang, Y. L.; Edwards, M. A.; McKelvey, K.; White, H. S.; Willets, K. A. Three-Dimensional Super-resolution Imaging of Single Nanoparticles Delivered by Pipettes. *ACS Nano* **2017**, *11*, 10529-10538.
43. Heintzmann, R.; Relich, P. K.; Nieuwenhuizen, R. P.; Lidke, K. A.; Rieger, B. Calibrating Photon Counts From a Single Image. *arXiv preprint* **2016**, *arXiv:1611.05654*.
44. Lan, W. J.; Kubeil, C.; Xiong, J. W.; Bund, A.; White, H. S. Effect of Surface Charge on the Resistive Pulse Waveshape during Particle Translocation through Glass Nanopores. *J. Phys. Chem. C* **2014**, *118*, 2726-2734.
45. Lan, W. J.; White, H. S. Diffusional Motion of a Particle Translocating through a Nanopore. *ACS Nano* **2012**, *6*, 1757-1765.
46. Lan, W. J.; Edwards, M. A.; Luo, L.; Perera, R. T.; Wu, X. J.; Martin, C. R.; White, H. S. Voltage-Rectified Current and Fluid Flow in Conical Nanopores. *Acc. Chem. Res.* **2016**, *49*, 2605-2613.
47. Schmeltzer, A. J.; Harris, J. M.; White, H. S. Single-Molecule Electrical Currents Associated with Valinomycin Transport of K^+. *ACS Nano* **2023**, *17*, 8829-8836.
48. Lind, T. K.; Wacklin, H.; Schiller, J.; Moulin, M.; Haertlein, M.; Pomorski, T. G.; Cardenas, M. Formation and Characterization of Supported Lipid Bilayers Composed of Hydrogenated and Deuterated Escherichia coli Lipids. *Plos One* **2015**, *10*, e0144671.
49. Wustner, D.; Solanko, L. M.; Lund, F. W.; Sage, D.; Schroll, H. J.; Lomholt, M. A. Quantitative fluorescence loss in photobleaching for analysis of protein transport and aggregation. *Bmc Bioinformatics* **2012**, *13*, 1-21.
50. Kobayashi, Y.; Misawa, K.; Kobayashi, M.; Takeda, M.; Konno, M.; Satake, M.; Kawazoe, Y.; Ohuchi, N.; Kasuya, A. Silica-coating of fluorescent polystyrene microspheres by a seeded polymerization technique and their photo-bleaching property. *Colloid Surface A* **2004**, *242*, 47-52.
51. Swoboda, M.; Henig, J.; Cheng, H. M.; Brugger, D.; Haltrich, D.; Plumeré, N.; Schlierf, M. Enzymatic Oxygen Scavenging for Photostability without pH Drop in Single-Molecule Experiments. *ACS Nano* **2012**, *6*, 6364-6369.
52. Cordes, T.; Maiser, A.; Steinhauer, C.; Schermelleh, L.; Tinnefeld, P. Mechanisms and advancement of antifading agents for fluorescence microscopy and single-molecule spectroscopy. *PCCP* **2011**, *13*, 6699-6709.

53. Gong, W. J.; Das, P.; Samanta, S.; Xiong, J.; Pan, W. H.; Gu, Z. Y.; Zhang, J. G.; Qu, J. L.; Yang, Z. G. Redefining the photo-stability of common fluorophores with triplet state quenchers: mechanistic insights and recent updates. *Chem. Commun.* **2019**, *55*, 8695-8704.
54. Mittman, S.; Flaming, D. G.; Copenhagen, D. R.; Belgum, J. H. Bubble Pressure Measurement of Micropipet Tip Outer Diameter. *Journal of neuroscience methods* **1987**, *22*, 161-166.

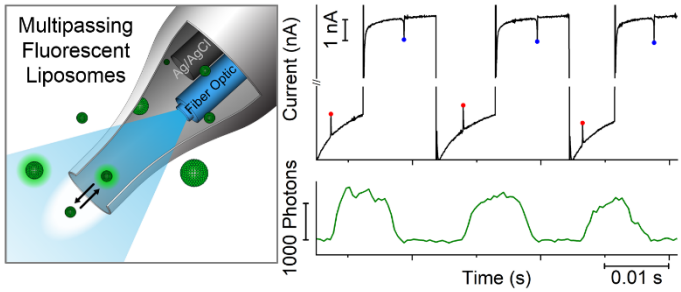

TOC Figure